

Generation and unstable evolution of a density-driven Eastern Poleward Current: The Iberian Poleward Current

Álvaro Peliz,¹ Jesus Dubert,² Dale B. Haidvogel,³ and Bernard Le Cann⁴

Received 17 April 2002; revised 17 April 2003; accepted 19 May 2003; published 21 August 2003.

[1] The generation and evolution of a density-driven Eastern Poleward Current is investigated using a high-resolution primitive equation numerical model. The simulations focus on the Iberian Poleward Current (IPC) as a case study. The flow is generated by a meridional upper ocean density gradient balanced by an eastward surface-intensified flow that adjusts at the coastal margin. The resulting current system has a baroclinic character with poleward flow at the surface layer, and equatorward flow underneath. A few weeks after initialization, the sheared along-slope flow generates several vorticity structures downstream of the main topographic features. In the lee of the topography, persistent anticyclones are observed and deep cyclogenesis is induced in relation to the meandering of the upper layer jet. These structures evolve preferentially as cyclone/anticyclone eddy pairs, and after interaction some dipoles are ejected offslope. Within a period of a few months, the initial meridional gradient evolves into a complex system of fronts, eddies and slope flows. The dynamics of flow topography interaction is analyzed. A comparison with satellite imagery of the IPC is conducted and similarity in scales and patterns is noted. *INDEX TERMS:* 4516 Oceanography: Physical: Eastern boundary currents; 4520 Oceanography: Physical: Eddies and mesoscale processes; 4528 Oceanography: Physical: Fronts and jets; *KEYWORDS:* Eastern Poleward Currents, Iberian Poleward Current, slope flows, topographic steering, mesoscale eddy shedding, sweddies

Citation: Peliz, Á., J. Dubert, D. B. Haidvogel, and B. Le Cann, Generation and unstable evolution of a density-driven Eastern Poleward Current: The Iberian Poleward Current, *J. Geophys. Res.*, 108(C8), 3268, doi:10.1029/2002JC001443, 2003.

1. Introduction

[2] A type of poleward flow circulates along midlatitude eastern continental margins driven by density forcing associated with larger-scale meridional thermal gradients. In the vicinity of the coast, these density gradients are balanced by onshore flow that adjusts at the slope/shelf generating surface-intensified currents oriented towards the poles. Examples of such flows are reported in different parts of the Western European margin [e.g., *Huthnance*, 1984] and Western Australia-Leeuwin Current [e.g., *Weaver and Middleton*, 1989]. These Eastern Poleward Currents (EPC) usually have long meridional extensions, even when generated in a relatively short coastal zone, and undergo strong topographic steering along the shelf/slope margin. Eddy structures are observed along these oceanic boundaries as trains of vorticity structures or single coherent eddies [e.g., *Griffiths and Pearce*, 1985; *Pingree and Le Cann*, 1992] related to the separation or evolution of perturbations in the flow regime.

[3] Modeling studies of EPC usually address the wind-driven component of the flow; however, high-resolution models of density-driven flows are still unexplored in the literature. This work presents a modeling study of the latter type of flow focusing on the Iberian Poleward Current (IPC).

[4] The IPC circuits the western and northern Iberia margins and is intensified during winter. It was first documented as a narrow slope-trapped tongue-like structure progressing northward and noticeable by a conspicuous warm signature in the SST imagery [e.g., *Frouin et al.*, 1990; *Haynes and Barton*, 1990]. Besides this topography-following character, the IPC exhibits a turbulent nature, and some unstable structures and separating eddies have also been reported in the bay of Biscay region [*Pingree and Le Cann*, 1993]. Figure 1 shows two examples of winter imagery of the western Iberia offshore, where it is possible to observe the meridional thermal gradient, the poleward propagation of warm waters along slope and several unstable structures. In the vicinity of the slope, the meridional gradients are deflected northeastward with the generation of anticyclones, dipole structures, and poleward slope flow creating a Coastal Transition Zone (CTZ).

[5] The present research aims to contribute to the understanding of the mechanism of generation of the IPC and to study its turbulent character. In particular, we investigate the origin and nature of the structures present in winter satellite images of the Western Iberia margin, like those shown in Figure 1. Numerical simulations of the CTZ forced by a

¹Instituto de Investigação das Pescas e do Mar, Lisboa, Portugal.

²Departamento de Física, Universidade de Aveiro, Aveiro, Portugal.

³Institute of Marine and Coastal Sciences, Rutgers University, New Brunswick, New Jersey, USA.

⁴Laboratoire de Physique des Océans, CNRS/IFREMER/UBO, Brest, France.

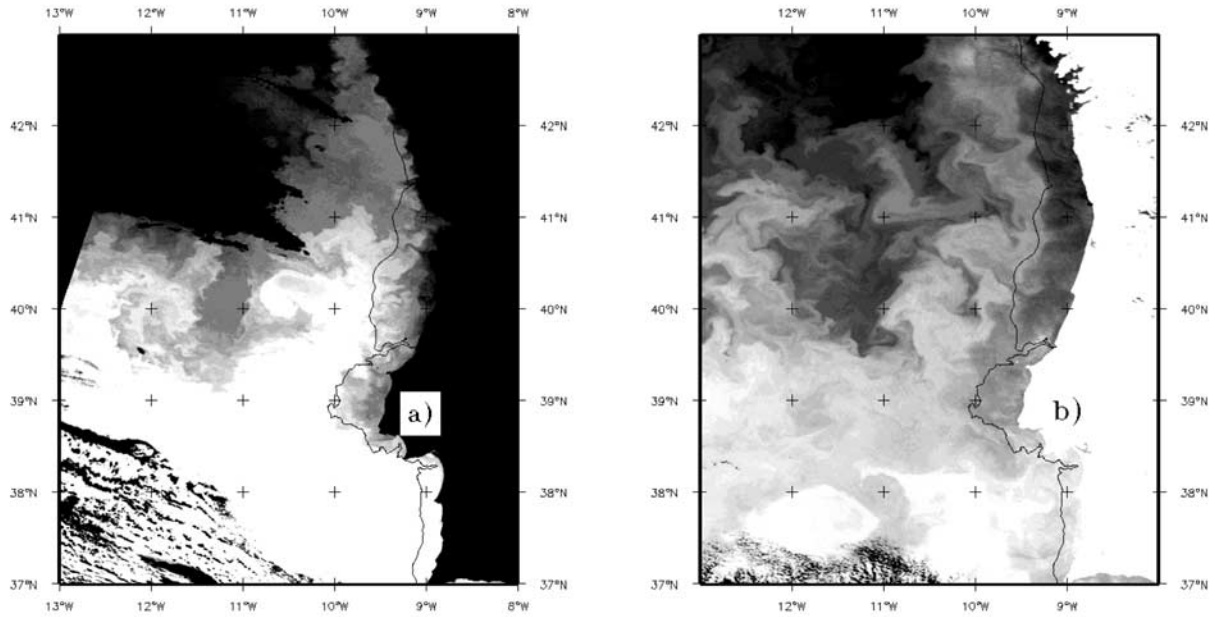


Figure 1. AVHRR channel 4 brightness temperature images of Western Iberia margin showing the Iberian Poleward Current. Lighter tones correspond to warmer waters. (a) 28/01/97 (0321 UTM). (b) 25/02/98 (1511 UTM). The black solid line represents the 200-m isobath. Owing to the temperature contrast, land portion is in black in the first image (Figure 1a) and in white in the second case (Figure 1b).

meridional density gradient with characteristics approximating to those of the winter period are discussed, and mechanisms of flow-topography interaction and eddy shedding are described. The modeled CTZ features are compared with observations, and an analysis of similarity in scales and patterns is given. Although the simulations focus on the IPC as a case study, the described processes have applicability in other EPC. Similar forcing, poleward flow, and turbulent structures are also found in other systems, for instance, in the Leeuwin current [Griffiths and Pearce, 1985; Weaver and Middleton, 1989, Figure 1].

[6] In the next section, the experimental setup is described. Section 3 is dedicated to the kinematics of the main experiment. In section 4, several dynamical processes are isolated and analyzed. We focus on flow topography interaction, deep cyclogenesis, and the detachment of dipolar structures. In section 5, a comparative analysis of the evolution of the flow in idealized slopes is provided. Section 6 is dedicated to comparison of scales and structures with satellite imagery and observations reported in other studies. Finally, discussion and conclusions are presented.

2. Experimental Set-Up

2.1. Meridional Density Gradient Forcing

[7] An overview of the winter upper ocean structure off western Iberia is presented by A. Peliz et al. (Winter upper ocean circulation off Western Iberia: Fronts, eddies and poleward flows: An overview, submitted to *Deep Sea Research*, 2003) (hereinafter referred to as Peliz et al., submitted manuscript, 2003). The meridional density structure is composed by an almost permanent large-scale density gradient [e.g., Arhan et al., 1994; Van Aken,

2001] together with occasional shorter-scale density differences associated with a zonally aligned front (denoted the Western Iberia Winter Front by Peliz et al. (submitted manuscript, 2003)) often observed in satellite imagery of the region. The location of this frontal system is variable but frequently observed between about 38°N and 40°N. Observational evidence of such gradients is presented by Pollard and Pu [1985], Mazé et al. [1997] and J. P. Vitorino (Resultados do cruzeiro CECIR XVII (CECIR XVII cruise report), unpublished manuscript, Instituto Hidrográfico, Lisbon, 1995). They constitute a transition of about 200 km between the southern stratified waters and the northern waters with deeper mixed layer typical of these latitudes. According to Pollard and Pu [1985], they may develop as a result of the convergence of warm/salty/stratified waters originating in the northern edge of the Azores Current, with the cold/fresher/mixed waters being advected southward by the Portugal Current. The gradient formulation used in the present experiments mimics the density structure observed in the hydrography survey described by Vitorino [1995]. The temperature and salinity fields are

$$S(y, z) = S_o + F_s(z) + 0.5 * \delta_{ss} G_1(y, z) + 0.5 * \delta_{sb} G_2(y, z), \quad (1)$$

$$T(y, z) = T_o + F_t(z) + 0.5 * \delta_{ts} G_1(y, z) + 0.5 * \delta_{tb} G_2(y, z), \quad (2)$$

$$G_1(y, z) = 1 + \tanh\left(\frac{z - \alpha y^6 - z_0}{d_0}\right), \quad (3)$$

$$G_2(y, z) = 1 + \tanh\left(\frac{-z - (z_1 - z_2 * 0.5 * (1 + \tanh(\frac{y - y_0}{y_1}))}{d_1}\right), \quad (4)$$

where, z is depth in meters, y is the meridional distance in meters, $T_0 = 13.0^\circ\text{C}$, $S_0 = 35.5$ (psu), $F_s(z) = 0.5 e^{z/400}$ (psu), and $F_r(z) = 0.003 z^\circ\text{C}$. The coefficients used are: $d_0 = 100$ m, $d_1 = 100$ m, $z_0 = -120$ m, $z_1 = 325$ m, $z_2 = 125$ m, $y_0 = 1.2 \cdot 10^5$ m, $y_1 = 0.3 \cdot 10^5$ m, $\alpha = -10 z_0 / (2.8 \cdot 10^5)^6$, $\delta_{ss} = 0.2$ (psu), $\delta_{sb} = 0.1$ (psu), $\delta_{ts} = 1.5^\circ\text{C}$, and $\delta_{tb} = 2.0^\circ\text{C}$.

[8] Using a nonlinear expression, a meridional (y, z) idealized density structure is obtained for the initialization of the numerical model inside the domain represented in Figure 2. The gradient is zonally uniform and is represented in Figure 3a only as a function of latitude and depth. The density structure is concentrated in the upper ocean (0–400 m) in the southern portion of the domain, and is in geostrophic balance with a surface-intensified current of about 0.07 m s^{-1} in the coastward direction (Figure 3a).

[9] This adjusted inflow condition at the western boundary is kept almost constant during all the simulations, as

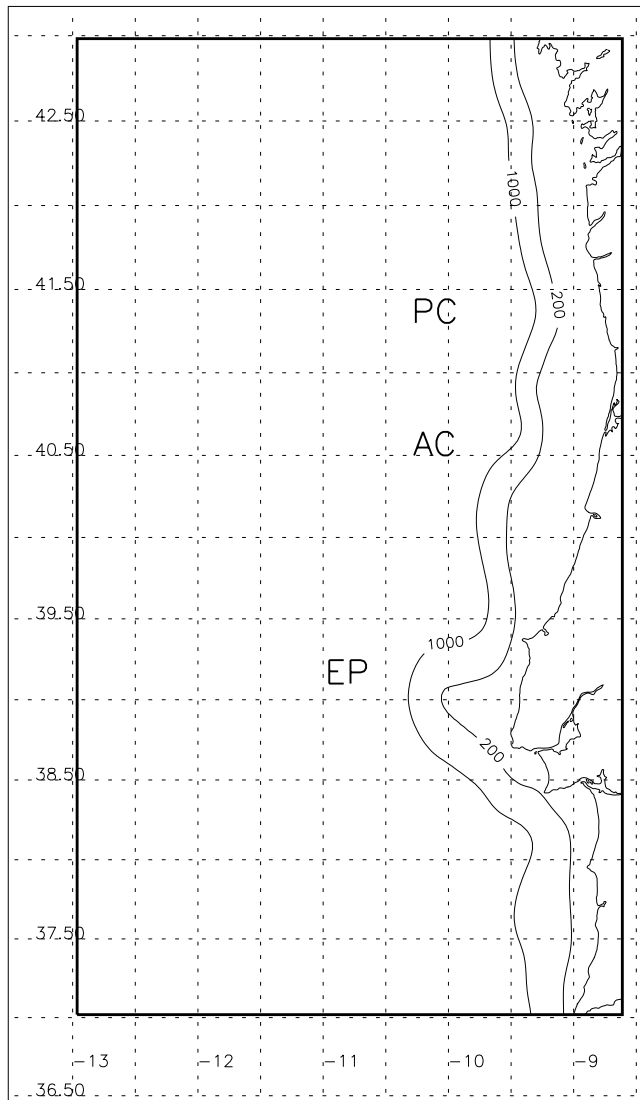


Figure 2. Domain of computation (inside the solid thick line) and topography (isobaths 1000 m and 200 m). The labels represent the main topographic features: EP, Estremadura Promontory; PC, Porto Canyon; and AC, Aveiro Canyon.

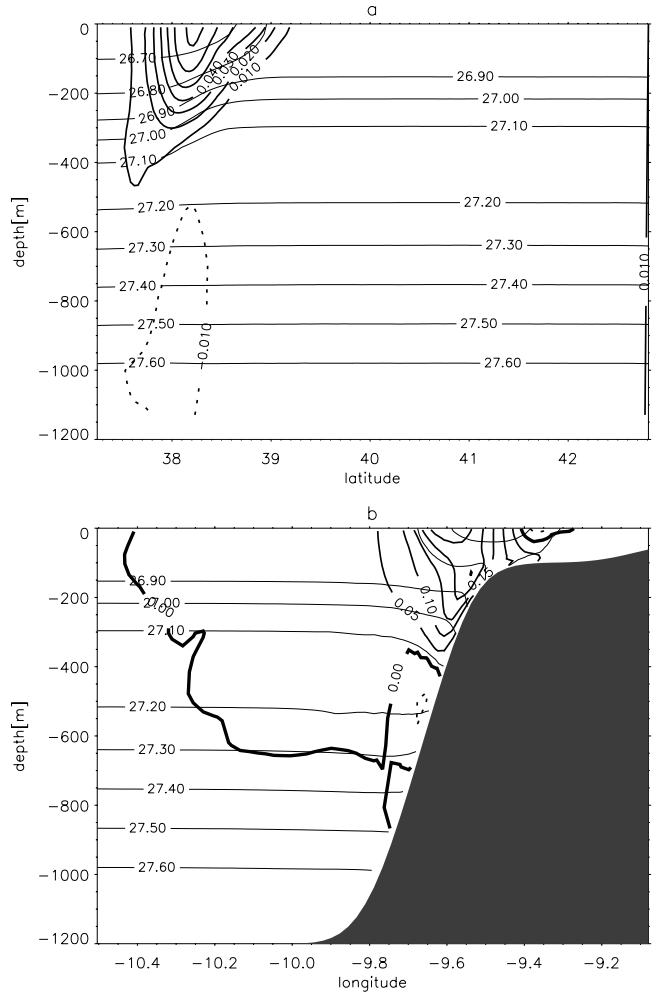


Figure 3. (a) Meridional (12°W) and (b) cross-slope (40.1°N) sections of the adjusted flow (day 20). The thin lines correspond to the density anomaly $[\sigma_t]$, and the thick lines to cross-section velocity $[\text{m s}^{-1}]$. In Figure 3a, solid (dashed) lines correspond to eastward (westward) flow. In Figure 3b, solid (dashed) lines correspond to northward (southward) flow.

described below. No other forcing is imposed and all the dynamics are consequence of the evolution of this initial gradient interacting with the shelf/slope.

2.2. Model and Configuration

[10] The experiments were conducted with a primitive equation model using a curvilinear, and terrain-following coordinate system (Regional Ocean Modeling System, ROMS [Haidvogel *et al.*, 2000]). The model domain is constituted by a meridionally oriented, midlatitude, channel-like basin approximately 660 km by 340 km (37°N to 43°N and 8.5°W to 13.5°W) as represented in Figure 2. The bathymetry is constituted by a shelf/slope system that approximates the real topography of the Western Iberia margin. Some smoothing is used in order to accommodate the bathymetric gradient under the required maximum r-factor of 0.2 [e.g., Haidvogel and Beckman, 1999] to avoid pressure gradient errors inherent in sigma coordinate models close to steep bathymetry. Off slope, the maximum

Table 1. Model Parameters Used in Central Experiment

| | | |
|--------------|---------------------------------------|---|
| L | 118 | number of points in the longitude direction |
| M | 164 | number of points in the latitude direction |
| N | 20 | number of s-levels |
| h_{max} | 1200 m | maximum depth of the domain |
| h_{min} | 22 m | minimum depth of the domain |
| θ_s | 3.0 | sigma coordinate stretching factor |
| θ_b | 0.2 | sigma coordinate bottom stretching factor |
| Δx | [1.7–6.7] km | resolution in the zonal direction |
| Δy | [3.5–4.1] km | resolution in the meridional direction |
| Δt | 480 s | baroclinic time step |
| Δt_f | 16 s | barotropic time step |
| ν | $5.0 \text{ m}^2 \text{ s}^{-1}$ | Laplacian horizontal viscosity |
| ν_t | $5.0 \text{ m}^2 \text{ s}^{-1}$ | Laplacian horizontal diffusivity |
| r | $3.0 \times 10^{-4} \text{ m s}^{-1}$ | linear bottom drag coefficient |

depth is set to 1200 m and the minimum depth at the coast is 22 m. ROMS allows the grid cell size to vary over the domain, and this feature is used to increase the resolution at the slope and shelf. This is important to better resolve the slope flow (the focus of the present research) in a better way and to enable the use of steeper (more realistic) slopes without significant pressure gradient errors. In the meridional direction the resolution is constant, about 4 km. Zonally, the resolution increases smoothly from offshore (around 6 km) to the shelf/slope (about 2 km).

[11] The bottom stress is parameterized using the linear relation $\tau_b = r v_b$ where v_b stands for the deepest level velocity, with $r = 3 \cdot 10^{-4} \text{ m s}^{-1}$. The vertical mixing scheme is based on the vertical closure turbulent model proposed by *Large et al.* [1994] (K - profile parameterization, KPP) and modified to represent the bottom boundary layer by *Durski* [2000]. Other parameters, such as those associated with vertical resolution and horizontal mixing, are described in Table 1.

[12] All boundaries are open except the eastern limit of the basin which represents the coast. At the western boundary, the inflow is kept quasi-steady by the use of relaxation terms in the equations inside a belt of six grid points. Along this nudging band, the time constants used in the restoring terms vary between 1 day at the boundary to 6 days in the interior. Active/passive boundary conditions [*Marchesiello et al.*, 2000] were also used at the boundaries together with the relaxation terms. To avoid the reflection and/or recirculation of the poleward flow strong nudging was applied to the inflow and outflow with a time constant of less than 1 day in both the momentum and tracer equations.

3. Main Experiment

[13] Figure 4 presents the evolution of the surface temperature field for the central experiment. To describe the kinematics of this current system we distinguish three stages. In the first 2–3 weeks (days 0–20), we observe adjustment of the geostrophically balanced onshore flow as a poleward current trapped to the slope. No significant eddy activity is noted, and the warm tongue following the bathymetry is the most recognizable signature of the flow field by the end of this period (see day 20). After this initial adjustment stage, eddy activity starts to be relevant, with the consequent detachment of the thermal front from the bathymetric contours and the development of meanders associated with flow structures induced by topographic irregularities

and as a consequence of instability (days 20–80). Finally, the unstable structures develop sufficiently for the interaction of existing eddies to begin, and the generation of other flow features like off-slope separation is observed (days 80–120).

[14] To follow the evolution of the unstable regime, mean (MKE = $0.5\rho_0\bar{\mathbf{u}}^2$) and eddy (EKE = $0.5\rho_0\mathbf{u}'^2$) kinetic energies were calculated using the definitions

$$\bar{\mathbf{u}} = \sum_i \sum_k \hat{\mathbf{u}}(x, z),$$

$$\hat{\mathbf{u}}(x, z) = \sum_j \mathbf{u}(x, y, z),$$

$$\mathbf{u}' = \sum_i \sum_j \sum_k \hat{\mathbf{u}}(x, z) - \mathbf{u}(x, y, z).$$

[15] The mean is assumed to be the along-shore averaged flow $\hat{\mathbf{u}}$, and the perturbations of the deviations from this mean along-slope current (all terms are normalized by the cell volume). This definition is based on the fact that the mean flow (nonperturbed by eddies) is essentially along the topography which is meridionally aligned. This assumption has drawbacks in the case of the experiment with real topography. However, the values obtained seem to be coherent and representative of the dynamics. Other definitions of mean and perturbed flow were tested with less clear results (energy balances requiring absolute values is not the scope of the present analysis).

[16] Time series of both quantities are presented in Figure 5 (solid curves). The eddy kinetic energy curve presents different slopes (small lines with numbers close to the curves) which also correspond to different phases of the unstable evolution. These will be analyzed below in relation to the stages defined above (represented with the shaded bars in Figure 5).

3.1. Adjustment Stage

[17] The imposed meridional gradient induces a surface-intensified eastward flow about 150–200 km wide in the 400 m surface layer with maximum onshore velocities around 0.07 m s^{-1} (Figure 3a). In the deeper layers, a small counterflow with maximum values of about 0.01 m s^{-1} in the opposite direction (off domain) is observed.

[18] The main consequence of the coastward flow is the generation of a tongue of southern lighter water progressing poleward at the surface (Figure 4). In the first days, the warm tongue mimics the topographic features with the isotherms following the bathymetry (see day 20, Figure 4). Over the shelf, there is evidence of a weak southward current (see the shelf zone in the cross-slope section of Figure 3b) induced by the baroclinic structure of the inshore side of the tongue. This shelf-edge current becomes unstable very soon with the generation of short-scale filamentation and tends to erode (it will not be analyzed further).

[19] The poleward flow is concentrated over the upper slope (about 0–400 m) and is bounded from below by the 27.1 isopycnal surface (Figure 3b). As more southern waters are being advected along the slope with the arrival of the warm tongue, the baroclinicity of the flow increases. The vertical shear is enhanced and the poleward flow intensifies (maximum values of about 0.30 m s^{-1}).

[20] Another important feature of the adjusted slope flow is the undercurrent observed in the velocity section of

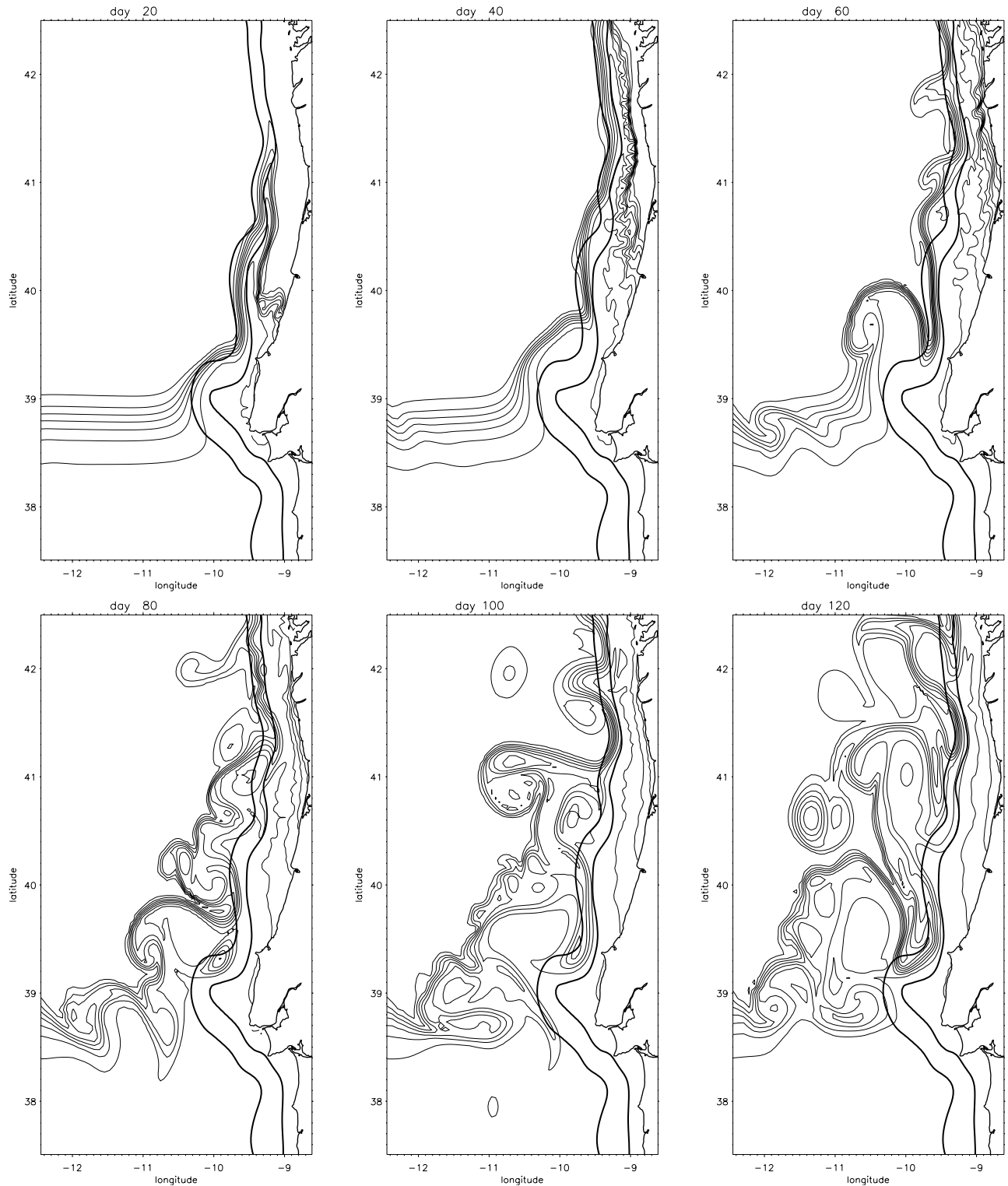


Figure 4. Surface temperature field evolution for days, 20, 40, 60, 80, 100, and 120 for the main experiment. Minimum, maximum and interval values are, respectively, 15.0, 16.2, and 0.2°C. The topography is represented by the 200- and 1000-m lines (thick lines).

Figure 3b. The current along isopycnals below about 27.1 reverses and by about day 20, weak equatorward flow around 0.05 m s^{-1} with a core at approximately 500 m is noticeable.

[21] The kinetic energy plots (Figure 5) show that the mean flow energy values rise immediately after the first days and then remain stable during the simulation. The influence of higher frequency dynamics (note the 3- to 4-day

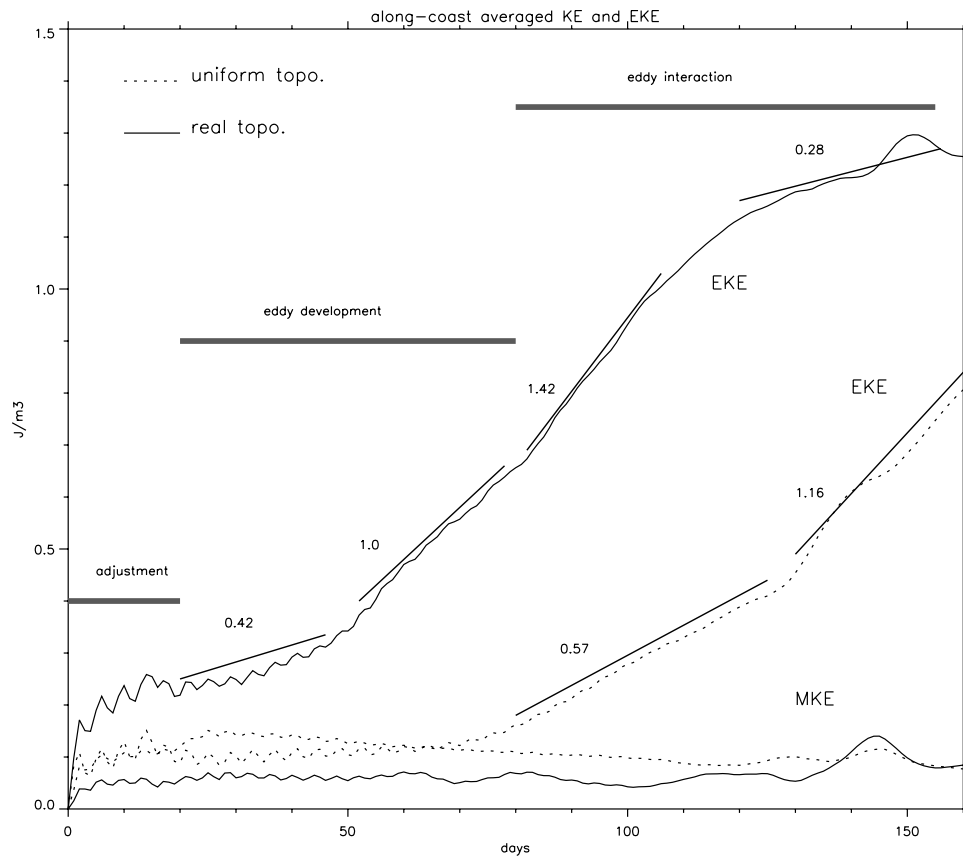


Figure 5. Time series of along-coast averaged kinetic energy (MKE) and eddy kinetic energy (EKE) for the experiment with realistic topography (solid lines) and with meridionally uniform topography (dashed lines). Shaded bars indicate the periods defined in section 3, and the small lines and numbers along the EKE curves were added to present some estimates of the slopes (10^{-2}).

fluctuations) in the first phase of adjustment probably associated with coastal trapped wave propagation is observed.

[22] The high values of eddy kinetic at the beginning partially reflect the definition of mean and perturbed flow as discussed previously. For the experiment with meridionally uniform topography (analyzed latter), that is not observed.

3.2. Eddy Development

[23] After the adjustment period, the poleward flow begins to respond to the topographic forcing. First, this is noticed by the way the temperature field decouples from bathymetry with the front being advected poleward (Figure 4, day 40). Later, the thermal front generates meanders associated with eddy activity.

[24] Hereafter, we follow the evolution of the flow field along two isopycnal surfaces which are representative of the upper and lower part of the current system: the 26.9 located at about 200 m, initially dominated by poleward flow, and the 27.2 (centered at 500 m deep) along which, after the initial adjustment stage, the flow is equatorward although weaker. The flow evolution along these surfaces is represented in Figure 6.

[25] The development of eddies was earlier discernible in the deeper layer close to the two most prominent bathymetric features: Estremadura Promontory (EP) and Aveiro Canyon (AC), shown in Figure 2. By day 20, two anti-

cyclones are noticeable: one to the north of the promontory (hereinafter PA1) and the second centered at the Aveiro Canyon (CA1). Both of these structures have a corresponding signal in the surface layer (26.9 isopycnal) which, although weak, represents an early tendency to separate off slope. The isopycnal fields for day 50 (Figure 6) show these vorticity features to be already well defined in the deeper layer. The anticyclonic eddy north of the Promontory is larger (about 60 km in diameter) than the one generated in the Aveiro Canyon. To the north, a third meander has developed at about 41.5°N (Figure 6, day 50) with an associated dipole on the 27.2 isopycnal (DC1 and DA1, cyclone and anticyclone, respectively). This latter feature originates at the Porto Canyon but it is not trapped to the topography and migrates northward. By day 50, this perturbation is located north of the canyon.

[26] The anticyclones shed in the lee of the main topographic features (with respect to the poleward flow) remain trapped for long periods, 2 to 3 months, and several smaller cyclones develop around them. On the 27.2 isopycnal surface (Figure 6, day 50), both anticyclones show a cyclonic eddy located upstream of the poleward current. This companion eddy is smaller and almost indistinguishable in the upper surface (26.9).

[27] Figure 7 presents the evolution of the 27.2 isopycnal depth and accompanying horizontal velocity every 5 days zoomed into the zone north of Estremadura Promontory

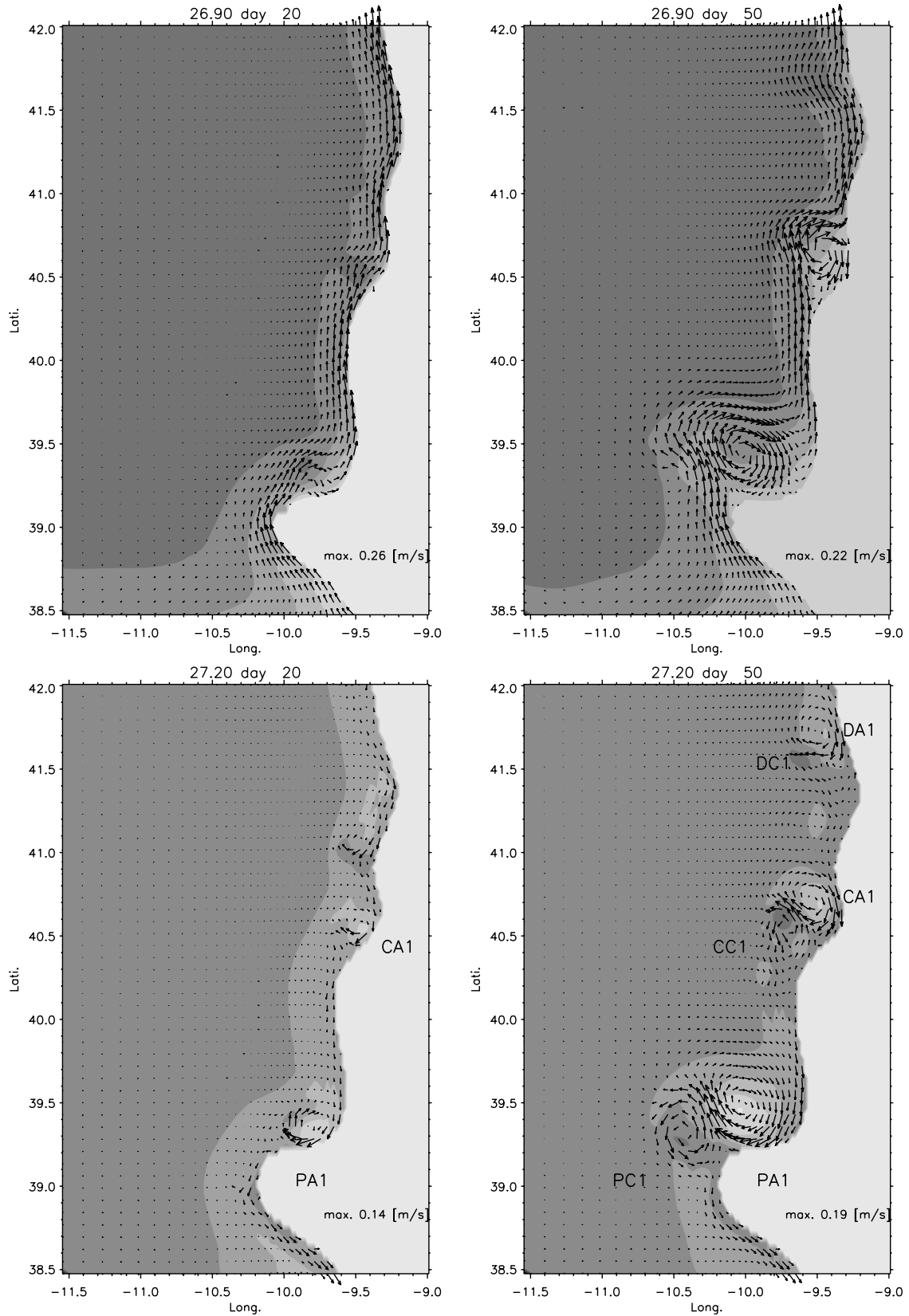


Figure 6. Depth of isopycnal surfaces (upper row 26.9 and lower 27.2) with lighter tones corresponding to deeper levels. Velocity vectors represent the flow along the isopycnal surface (vectors are plotted with half the resolution and maximum for the isopycnal is shown in the lower right corner). Plots are given for days 20, 50, 70, and 110 (columns). Labels indicate some of the eddies discussed in the text.

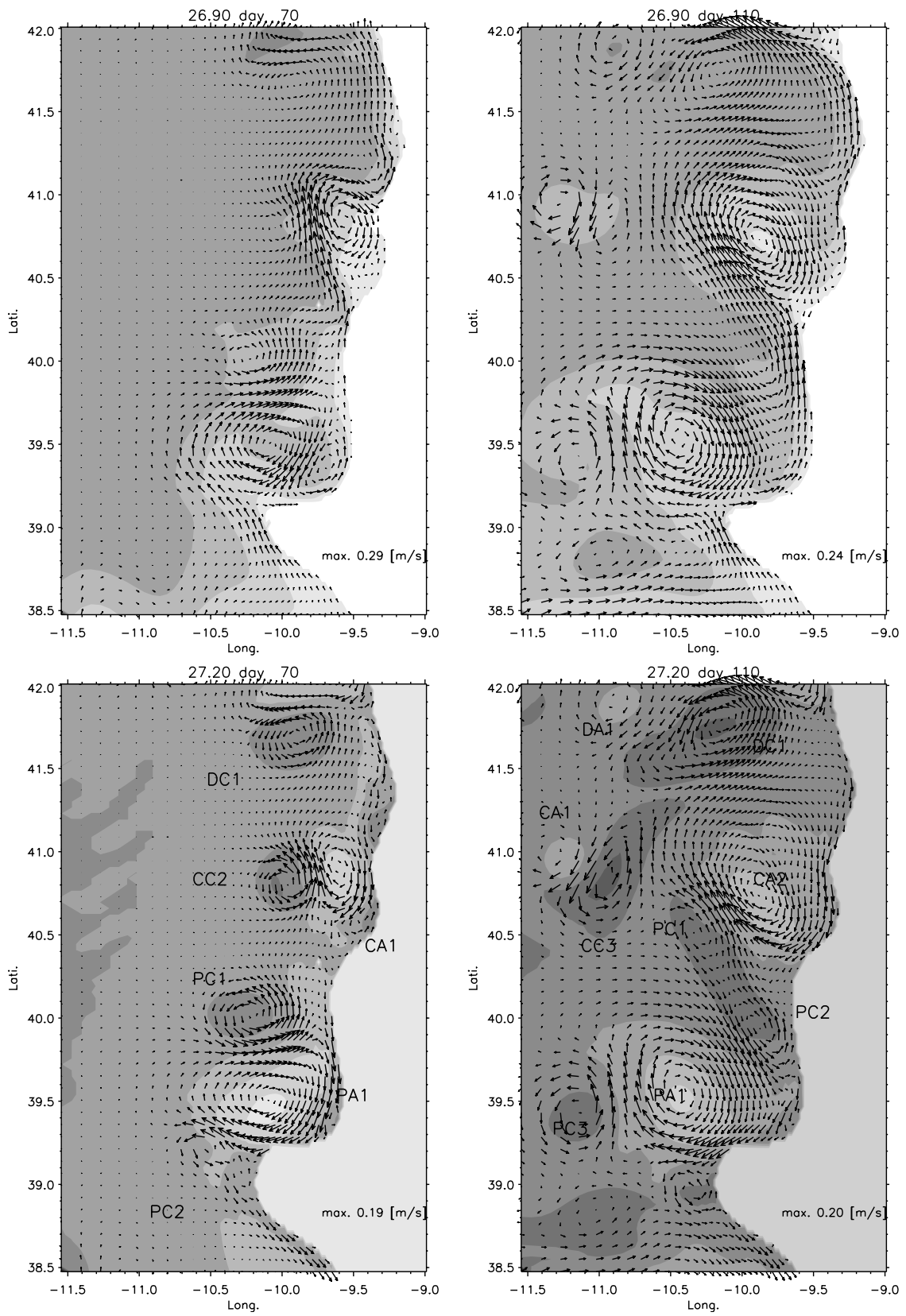


Figure 6. (continued)

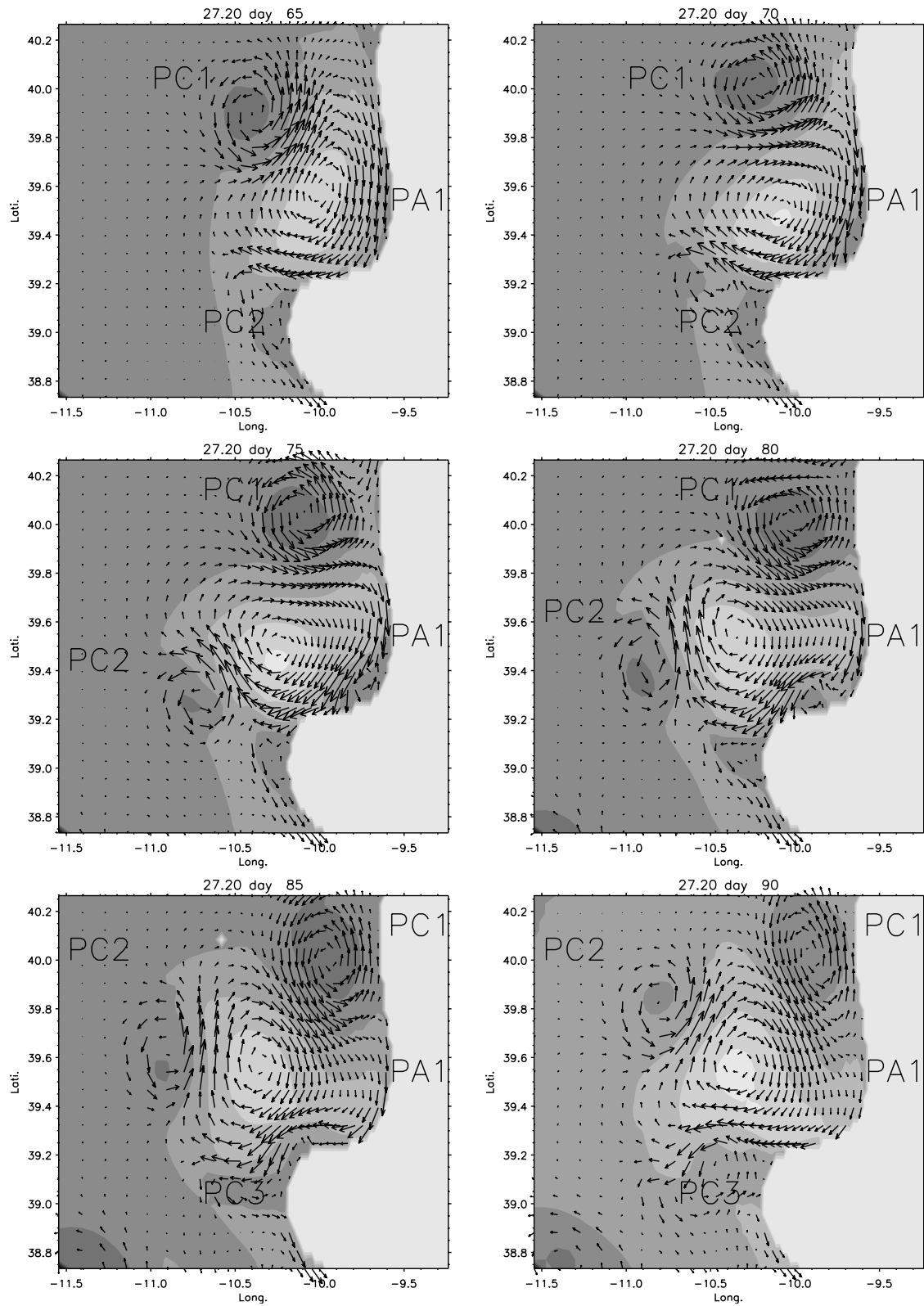


Figure 7. Depth of 27.2 isopycnal surface (lighter tones correspond to deeper pressure levels) and isopycnal velocity vectors, to the north of the Estremadura Promontory showing the generation of cyclones. Velocity vectors are plotted with half of the resolution and are not in scale. Labels indicate the location of the eddies discussed in the text.

where PA1 is centered. The cyclones are originally shed at the southern side of the anticyclones and rotate anticyclonically around them due to their weaker circulation. In the case of PA1, three complete events were registered. The first eddy pair constituted by PA1 and a smaller cyclone PC1 is detected on the 27.2 isopycnal surface by day 50 (see day 50 in Figure 6). In about 15 days (day 65 of Figure 7), PC1 has circuited PA1 and another cyclone PC2 is being shed. After that, both PC1 and PC2 continue circuiting PA1. In about 20 days, PC1 has reached the slope, PC2 finds itself north of PA1 and a third cyclone is generating.

[28] The shedding period of cyclones is about 20 days, and the generation of eddies at the promontory is a continuous process (PC3 was starting its cycle) but at advanced stages of the simulation, other flow interactions become important. In the case of the Aveiro Canyon, a similar process occurs. Here three cyclonic eddies (CC1, CC2, and CC3) are generated and encircle the anticyclone in a period of about 15 to 20 days.

[29] Although this cyclogenesis process is clear in the lower isopycnal surface (27.2), what is observed at the upper layer, the 26.9 isopycnal, is a meandering of the separated jet. Its orientation shifts between northwestward and northeastward periodically, and these flow patterns have associated cyclones in the deeper layers. The dynamics of this interaction is addressed below.

[30] The deep cyclogenesis has a signature in the evolution of the EKE (see Figure 5). The change in slope observed by day 50 (from $0.42 \cdot 10^{-2}$ to $1.0 \cdot 10^{-2}$), indicating that a growth of eddy activity is associated with the shedding of the cyclones in the deeper layer that begins around that period (see Figure 6).

3.3. Eddy Interaction

[31] After day 80 (Figure 4), flow interactions between the structures described before become noticeable. The eddies developed in the process of separation interact along the slope generating new flow structures. On the other hand, the instabilities of the zonal flow have developed enough to disturb and merge with the cyclones and anticyclones generated in the preceding stage.

[32] It is not possible to track each individual structure and to report its life history. It is worth noting, however, some of the main characteristics of these flow interactions. Three features should be highlighted. First is the global prevalence and robustness of anticyclonic circulation. Some of the features are absorbed or dissipated in the anticyclones. Note, for example, how PA1 (larger structure at about 10.5°W and 39.5°N in Figure 4 from day 60 to 120) undergoes several interactions with the structures generated in the zonal unstable flow without significant change. A second feature to be noticed is the way the flow organizes into three larger structures consisting of anticyclones interleaved with cold intrusions, reminiscent of an unstable event with one dominant wavelength (in this case of about 150 km). Finally, interaction mechanisms contribute to the separation of eddies off the slope. The most striking example is the fate of CA1. This anticyclone and its cyclonic companion have described a curved trajectory offshore ending about 150 km west of the slope. All these mechanisms contribute to a reorganization of the meridional gradient and the generation of a CTZ which, as will be seen

later in a comparison with satellite imagery, bear a great resemblance to real flow patterns.

[33] Finally, the evolution of the EKE curve during the eddy interaction stage (Figure 5) presents significant changes in slope. By day 80, the beginning of this period, the increase in the rate of eddy energy growth (the maximum for all the experiment) is associated with the beginning of the dipolar interaction that exports eddy flow off the slope (the enlargement of the area dominated by unstable flow). However, by about day 110, the area dominated by unstable flow stops growing and lower generation of EKE is observed (compare days 80, 100, and 120 in Figure 4).

4. Flow Separation and Eddy Shedding

[34] In the preceding section, a description of the kinematics of the adjustment of the meridional density gradient and the generation of the unstable EPC was given. Some interesting features merit a deeper analysis to highlight the dynamical processes resulting from the flow-topography interaction. The initial separation processes, the development of deeper structures, and the detachment of structures from the slope region will now be analyzed.

4.1. Flow Separation

[35] The poleward slope-trapped current resulting from the adjustment of the onshore flow shows a tendency to detach from the bathymetry at well-defined locations, mainly downstream of the topographic promontories. For instance, in Figure 6, along the isopycnal 26.90 by day 20, the detachment of the flow is visible downstream of Estremadura Promontory (EP) and past the southern flank of Aveiro canyon. This detachment process shows some resemblance to the behavior reported by *Klinger* [1994a]. In that work, laboratory experiments were conducted to investigate the generation of anticyclonic gyres by separation of a surface current from the coast in a rotating two-layer system. *Klinger* [1994a] shows the existence of a critical angle made by the corner (with respect to the incident upstream current) for separation. This angle should be above 40° – 45° , and for angles below those critical values, the profile of the current downstream of the corner changes as a function of the corner angle. It is also reported that the sensitivity of the detachment processes is attributed to the depth of upper and lower layers, and to the presence of bottom bathymetry. A key result of *Klinger* [1994a] is the generation of a cyclone, companion to the downstream anticyclone, which is responsible for the ejection of the dipole offshore. Even if our model stratification and bathymetry is rather different from *Klinger's*, there are a set of common features like the separation of the flow downstream of EP, the generation of anticyclones at the southern flank of AC, and the development of cyclonic vorticity, as described above.

[36] Other models of flow separation in oceanographic problems usually address the interaction of boundary flows with sharp topographic/coastal variations like outflows of channels and straits [e.g., *Whitehead and Miller*, 1979; *Bormans and Garrett*, 1989; *Nof and Pichevin*, 1999], where the problem enables the establishment of critical scales for flow separation or for the dimensions of gyres that generate past the obstacles. In the present case, the applications of these studies is limited. *Klinger's* [1994b]

theoretical work on the inviscid separation at rounded coastal bends is apparently closer to the conditions observed close to Estremadura Promontory in the beginning of the simulation (though Klinger's study uses reduced gravity model with flat bottom). Klinger established two critical radii of curvature for flow separation at a coastal rounded cape. One is for a current intensified near the coast,

$$\rho_c = \frac{u}{f} \frac{W}{R_d},$$

where R_d is the internal deformation radius and W the width of the current, and a second is for a flow intensified offshore (at a front),

$$\rho_c = \frac{u}{f}.$$

Using the results of day 20 (before separation) at the mid-slope off the promontory we can estimate the critical curvatures for inviscid separation.

[37] Using a crude estimate for the internal deformation Radius $R_d = 12$ km, $W = 30$ km for the width of the current, and an average flow speed of about $U = 0.12$ m s⁻¹, we obtain critical curvatures of about 2.2 and 0.8 km, which are well below the estimated curvature radius of the promontory (~12 km). The inertial inviscid separation is unlikely the central process in our case. The flow separation is a consequence of the process of eddy-topography interaction that will be analyzed next using potential vorticity arguments.

4.2. Deep Cyclogenesis

[38] To describe the process of eddy shedding in detail, we focus on the event north of the promontory for days 40 and 50, leading to the generation of PC1. Figures 8 and 9 represent the anomaly depth of the 27.2 (lower) and 26.9 (upper) isopycnal surfaces together with the corresponding isopycnal velocities. On the right side, the layer thickness anomaly is represented (thickness is defined as being the vertical distance between two isopycnal values $\rho_{ref} \pm 0.02$ kg m⁻³, where ρ_{ref} might be either 26.9 or 27.2).

[39] The use of the anomalies, rather than the absolute values, provides clearer visualization of the gradients. The anomalies are relative to the mean of the represented area. In the isopycnal surface depth anomaly fields (Figures 8a, 8c, 9a, and 9c), thicker/thinner lines correspond to shallower/deeper isopycnal levels, respectively. In the layer thickness anomaly fields (Figures 8b, 8d, 9b, and 9d), solid/dashed lines correspond to a thicker (stretched)/thinner (squeezed) water column.

[40] In the lee of the promontory, the flow turns anticyclonically and the 26.9 isopycnal becomes deeper and thicker inside of PA1 as indicated by the thickness maximum at the north of the promontory for day 40 (solid lines in Figure 8b). In the deeper layer (Figure 8d), the effect is the compression of the flow (note the change in the sign of the layer thickness anomaly) enhancing the anticyclonic circulation at those levels.

[41] As the deeper flow (27.2) circuits the northern border of the promontory equatorward, it is forced to cross a strong gradient in the layer thickness (see day 40 for 27.2 in Figures 8a and 8d). The water parcels stretch and acquire

positive vorticity as they flow perpendicular (offshore) to the upper layer jet which is flowing northward (compare the flow orientations on both levels for day 40) thus generating the deep cyclonic vorticity. By day 50, the cyclone is a clear structure in the 27.2 isopycnal surface as indicated by the depth anomaly centered at $x = 35$, $y = 60$ km (Figure 9c). At this time the flow is no longer crossing thickness gradients but tends to flow along them and the cyclonic vorticity production ceases. In the upper surface, the poleward flow is oriented slightly in the offshore direction (Figure 9a). Owing to the lower circulation, the released cyclone (Figure 9c) is advected by the anticyclone reaching again the slope by day 70 (Figure 6) and, in this process, the upper jet turns coastward again creating the conditions in the lower layer for the release of a second cyclone.

[42] This mechanism induces the wave pattern and oscillations of the upper separated jet that is associated with deep cyclogenesis. Figure 10 shows a schematic diagram of the phases of this cyclogenesis process. The large shaded arrow represents the poleward flow, whereas the small black arrows represent the circulation in the lower layer. In the first phase, the undercurrent crosses the thickness lines (dashed lines) and generates the cyclone. Next (phase 2) the cyclone is advected poleward along the offshore side of the upper jet. The jet undergoes an offshore turn and the thickness field is modified. Once the cyclone approaches the slope, the poleward flow returns to its original place and the shedding of a new cyclone begins.

[43] The shedding period is about 20 days, and three complete events past the promontory (another three at Aveiro Canyon) are detected in this experiment. With this value for the frequency n , an estimate of the curvature radius l of about 20 km, and a reference value for the velocity U of about 15 cm s⁻¹, the estimated Strouhal number $S = nl/U$ of this flow interaction is calculated to be approximately 0.08. An approximated value (0.1) was used by *Pingree and Le Cann* [1992] to estimate the rate of Slope Water Oceanic eddies (swoddies) production at Cape Ferret.

[44] The cyclogenesis could continue if no modifications occurred downstream of the promontory. However, other flow interactions become important as described above.

4.3. Dipole Detachment

[45] The clearest example of isolated anticyclones is CA1 (see Figure 6). Detachment occurs between days 90 and 100 and is shown in Figure 11. The figure shows the depths and velocity fields along the isopycnal surfaces (26.9 and 27.2). In the surface layer (left column), it is possible to observe the evolution of a surface meander into a dipole structure that ends up separating. The poleward jet is pushed offshore as the meander evolves into a filament-like structure (days 80 to 90). Finally, by day 100, the jet breaks and generates a second anticyclone inside the canyon (CA2). The corresponding flow structure in the deeper layer (right column), shows the generation of a cyclone inside the canyon (CC3). In relation to the meandering of the surface jet, the deeper equatorward flow is intensified (about 0.15 m/s) and separates offshore at the northern edge of the canyon (~9.5°W, 41.0°N). Consequently, a strong cyclone is generated (CC3). In the next days, the cyclone grows, reaching a diameter of about 50 km, which is comparable to the anticyclone. For this reason, it will influence the way the dipole structure evolves. Once the

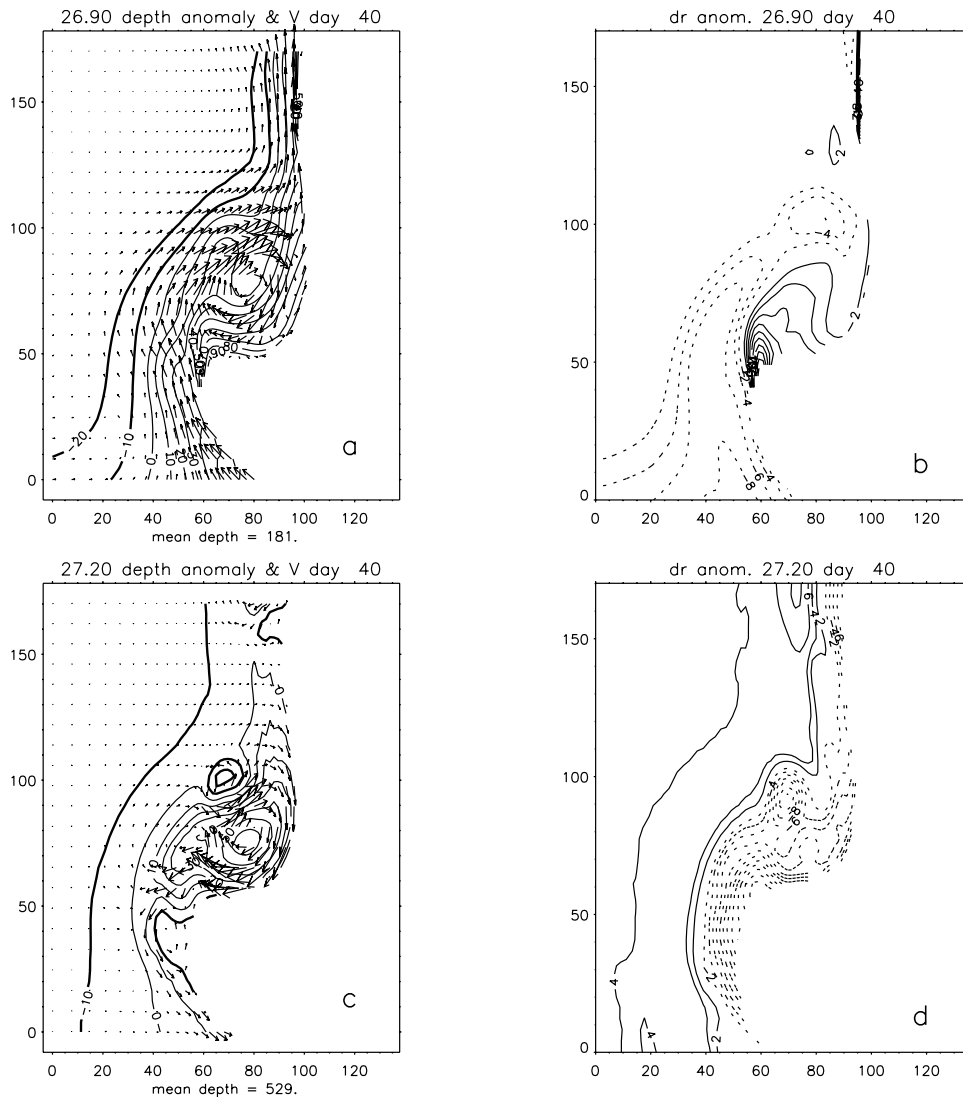


Figure 8. (a) Depth anomaly of 26.9 isopycnal surface (every 10 m) and the corresponding isopycnal velocity vectors in the lee of the promontory (the axis is in kilometers). The anomalies are calculated relative to the mean depth of the area visible in the image (the value is indicated in the x axis and thin lines correspond to deeper values). (b) Layer thickness anomaly for the 26.9 isopycnal value is plotted every 2 m (see text for definition). Solid lines correspond to thicker layer (stretched). (c, d) represent the same as Figures 8a and 8b for the lower (27.2) layer. All plots correspond to day 40. Note that vectors are not in scale.

cyclone starts moving offshore (see both surface and deeper layers for day 90) the upper jet separates from the northern edge of the canyon and CA2 is generated. The interaction between the cyclone and the anticyclone (see fields of day 100) provide further conditions for the separation of the dipole.

[46] In summary, Aveiro Canyon provides conditions for the separation of the upper flow and generation of anticyclones. Alternatively, at the northern edge of the canyon, the equatorward flow may separate and generate intensified cyclones in the deeper layers. In the situations presented before (section 4.1), the anticyclonic component usually dominated the dipolar structures. In this case, the cyclone is larger and influences the fate of the dipolar structure. It should be noticed that in both cases of detached dipoles, (CA1, CC3) and (DA1, DC1), the cyclonic component in

the lower layer is larger than the anticyclonic one (compare structures on the 27.2 isopycnal of day 110 in Figure 6).

[47] After the dipole is ejected offshore, its positive vorticity component then starts interacting with the offshore edge of another dipolar feature that is being generated upstream of the canyon (see Figure 4, days 100 and 120). This interaction deflects the dipole axis meridionally and it begins to self-advect southward. The anticyclonic component is surface intensified whereas its cyclonic counterpart dominates the deeper layers.

5. Experiments With Uniform Topography

[48] There are other perturbations along the poleward flow where the role of topography is not clear or not decisive in their evolution. The northernmost dipole struc-

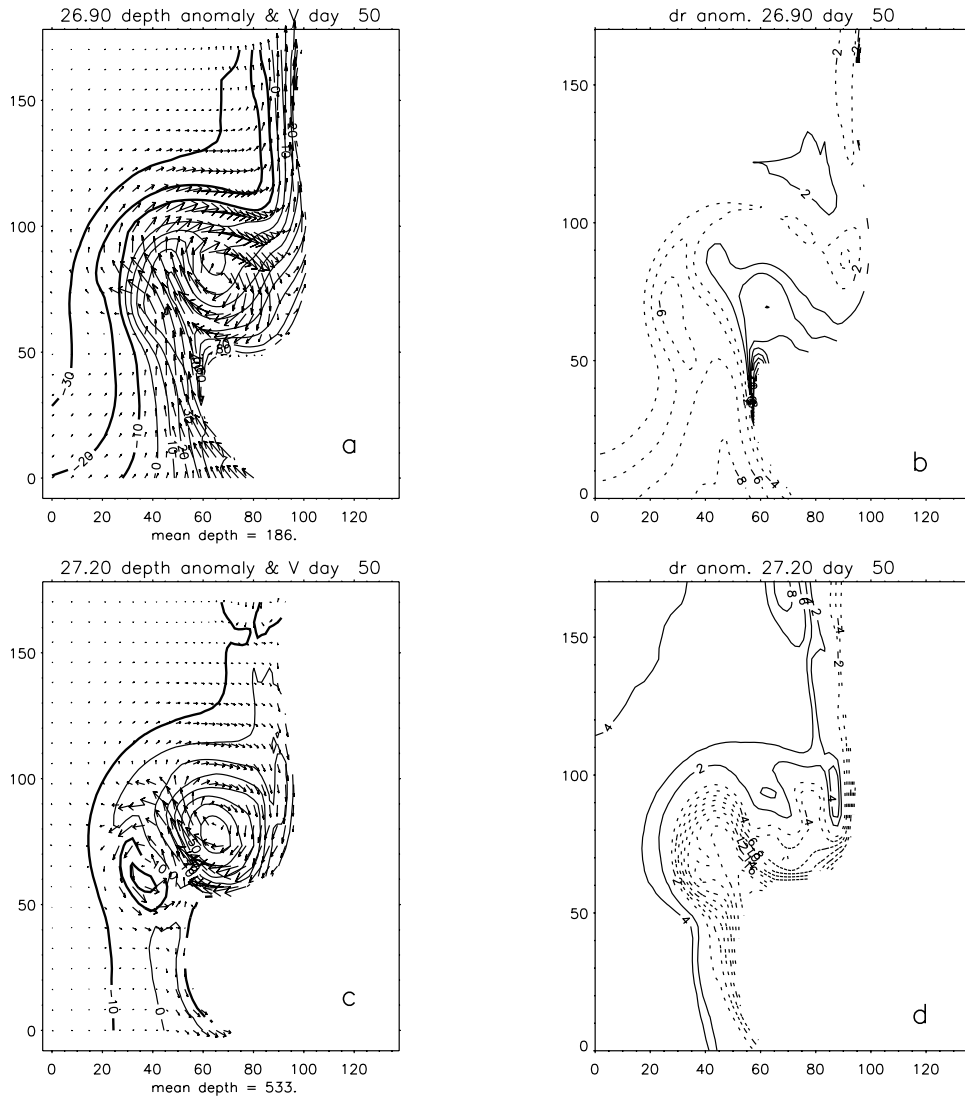


Figure 9. Same as Figure 8 but for day 50.

ture (DA1 and DC1 in Figure 6) starts developing as a small perturbation in the equatorward flow visible by day 20 in the 27.2 isopycnal surface (Figure 6). Part of this feature dissipates, but a residual of it starts developing as an eddy pair. By day 70, in the lower layer, the dipole is already a clear structure and is coincident with an offshore-oriented jet that has slowly progressed northward. By day 110, the dipole has migrated off slope and the anticyclone has become a separated structure (Figures 4 and 6). At this stage, a second instability takes place. In these cases, there is no generation of several cyclones as in the case of the trapped instabilities and the anticyclones evolve with their companion cyclone.

[49] These observations lead us to conclude that some differences might exist between the topographically induced instabilities described in the preceding subsections and the ones referred to above. In order to isolate the effect of bathymetric features in the flow evolution, other experiments were conducted with a simplified topography. In a configuration with a meridionally constant slope and straight coastline, instabilities are also observed, but considerably later (day 80).

[50] The instabilities (not shown) start as a small perturbation in the surface flow. In the deeper layers this perturbation corresponds to a small anticyclone that in the following days develops a cyclone generating an eddy pair that is slowly advected poleward with propagation speeds of about 0.02 m s^{-1} . In conclusion, these instabilities are mainly constituted by a meandering of the poleward flow at the surface with interacting cyclone/anticyclone pairs which are clearly seen in the lower layer. It is thus a dipolar structure with a dominating negative vorticity component. However, the components of the eddy pair remain attached between themselves and evolve in parallel with less interaction with other structures and consequently not separating offslope.

[51] Despite these differences, in a larger perspective, the final flow structure bears some similarities with the one obtained in the main experiment. Figure 12 shows the surface temperature and velocity fields for the experiment with realistic topography (upper row, days 100 and 120) and for the one with uniform slope (lower row, days 120 and 160). The purpose of showing different stages for the different experiments is to enable contrasting of the periods of development of the unstable structures. In both cases, the

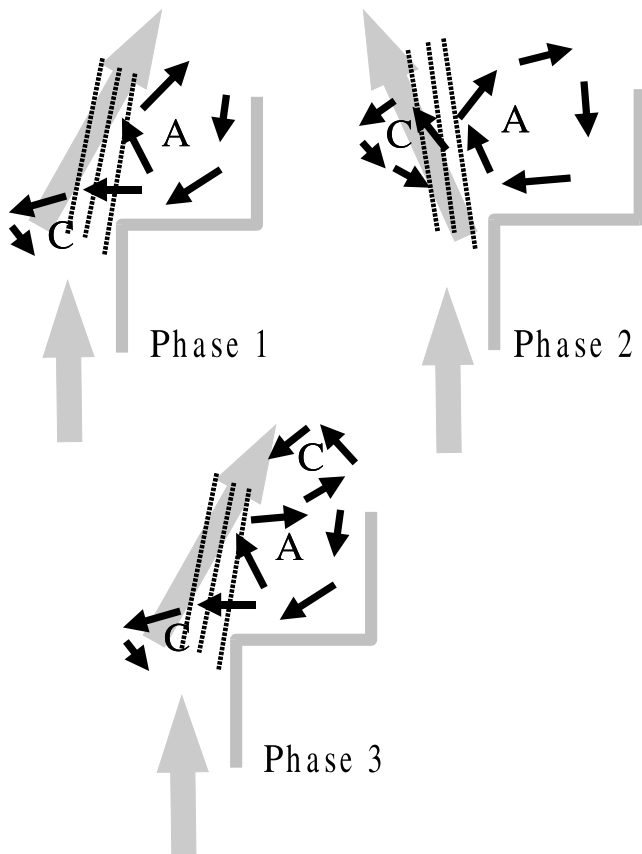


Figure 10. Schematic representation of the deep-cyclogenesis process. Shaded arrows represent the poleward surface flow, small black arrows represent the lower layer flow, and the dashed lines represent the thickness layer gradients.

flow is organized in several anticyclones inside the CTZ, but it should be stressed that this flow state is reached somewhat later in the run with uniform topography (compare days 120 and 160, Figure 12). Note that the similar stage of development of the structures for day 120 of the central experiment are only observable by day 160 of the constant slope experiment. Besides, the main experiment has developed several detached eddies that are absent here, although they might develop at latter stages of simulation.

[52] The differences in the two experiments are also apparent in the eddy kinetic energy plots of Figure 5. The time series for the experiment with uniform bathymetry are represented with a dashed line. Note that EKE for this experiment has considerably lower values than that with a realistic topography (solid line). The periods of different energy growth presented in the beginning of section 3 for the main experiment, are somewhat different for this case. Significant increase of EKE and a divergence from the MKE curve is only noticeable after day 70. A change in slope of the EKE curve towards higher growth rate happens by about day 130 when the experiment with real topography has entered the phase of eddy interactions with lower development of new kinetic energy. It is possible to say that the development of the EKE for the experiment with uniform topography was delayed by 40 days.

[53] Lastly, the alignment of the main instabilities is somewhat different in the results (Figure 12); compare day 120 of real topography run with day 160 of uniform topography. In the former case, the dipole axes are more meridionally aligned than in the constant-slope experiment and the cyclonic cold intrusions present a filamentary structure oriented in the north-south direction at advanced stages of the simulation. This may be due to the relative importance of the cyclone/anticyclone pairs in both experiments. In many cases, the flow-topography interaction gives rise to the development of intensified cyclones that strongly condition the fate of dipoles (including the separation). Finally, it is noticeable that at advanced stages of adjustment, the experiment with uniform bathymetry generates very large anticyclones that are not observed in reality. Similar features develop in the experiments with no bottom drag.

6. Comparison With Observations

[54] Availability of direct winter period current observations off western Iberia are rare. However, the few observational studies with information on the Iberia Poleward Current generally agree on the scale and intensities of the flow and support the values obtained in the present modeling experiments. Two earlier works on the IPC [Frouin *et al.*, 1990; Haynes and Barton, 1990] report very similar values for the width of the current (~ 30 to 40 km) and poleward surface velocities of about 0.2 to 0.3 m s^{-1} . A more comprehensive collection of current meter data along the Western Iberia slope zone is presented by Huthnance *et al.* [2002]. The values reported in this work are slightly less in intensity (~ 0.1 m s^{-1}) but they correspond to bimonthly means of vertically averaged (0 – 600 m) velocities. Martins *et al.* [2002] present statistics of five drifting buoys that were deployed in the beginning of winter in the northwestern Iberian slope zone. The mean speed of this set of drifters in its poleward progression was 0.151 ± 0.044 m s^{-1} . Although, many of these observation results come from indirect estimates and part of the direct measurements may have been taken out of the core of the IPC, it is possible to say that they provide a velocity scale for the current of about 0.2 to 0.3 m s^{-1} . The presented modeling results are noticeable within this range of absolute velocities as they are in many of the plots (e.g., Figures 6 and 12).

[55] Oliveira *et al.* [2003], report a high-resolution hydrology survey conducted in the area of Aveiro Canyon. Figure 13 presents a schematic of the circulation features estimated by the geostrophic calculations. In these observations, a poleward flow strongly perturbed by mesoscale eddies is apparent. The maxima of estimated velocities are about 0.15 to 0.20 m s^{-1} , and the spatial scales of the eddies are very similar to the ones obtained in the simulations. Similarity in the scale and positioning of the eddies may be noted by comparing with Figure 11. The spatial extent and distribution of the cyclones and anticyclones in the observed field is particularly close to the modeled structures of day 90 in Figure 11 (note the different longitudinal ranges of both figures). Note also the fact that in the surface layer (surface- 27.1 σ_θ), in the case of Oliveira *et al.* [2003] estimates, the continuity in the poleward flow seems to be present. However, that continuity is not so evident in the lower

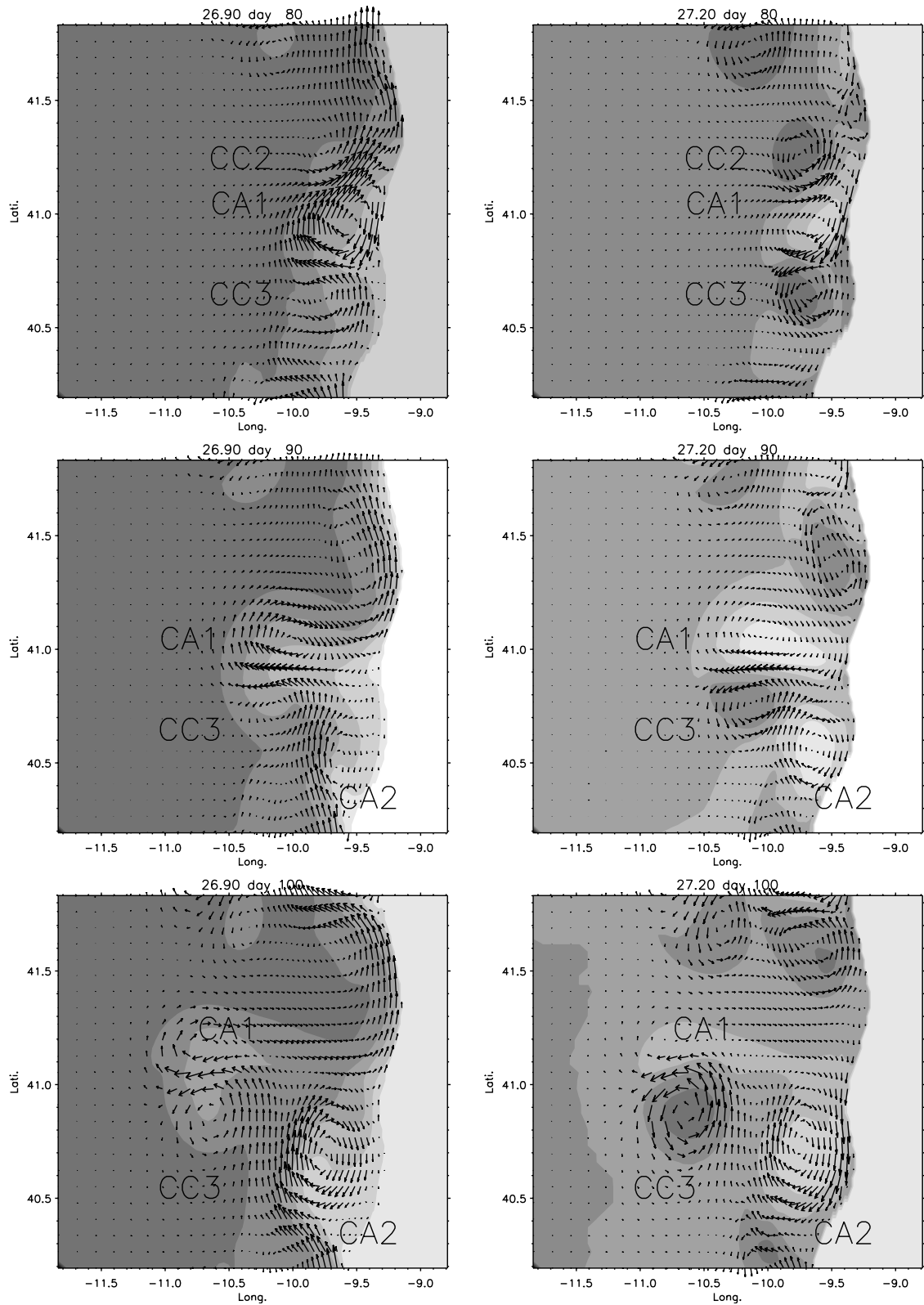
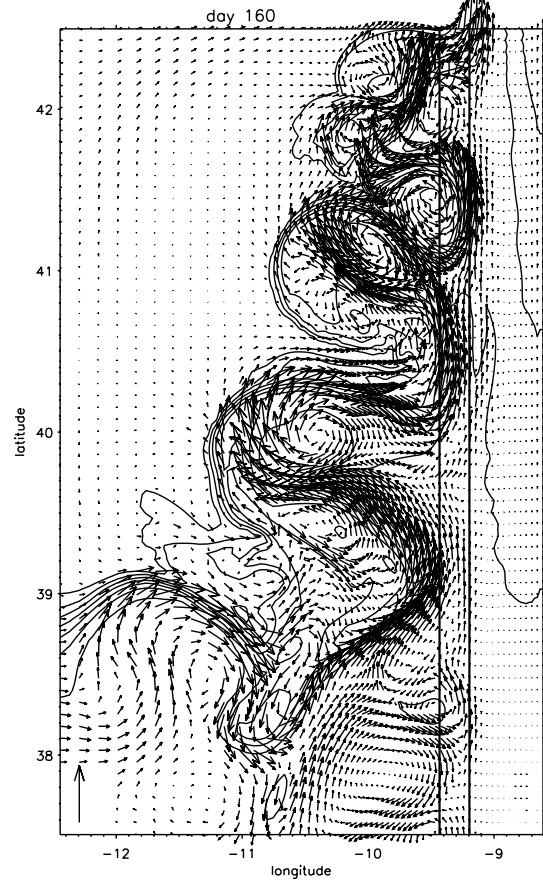
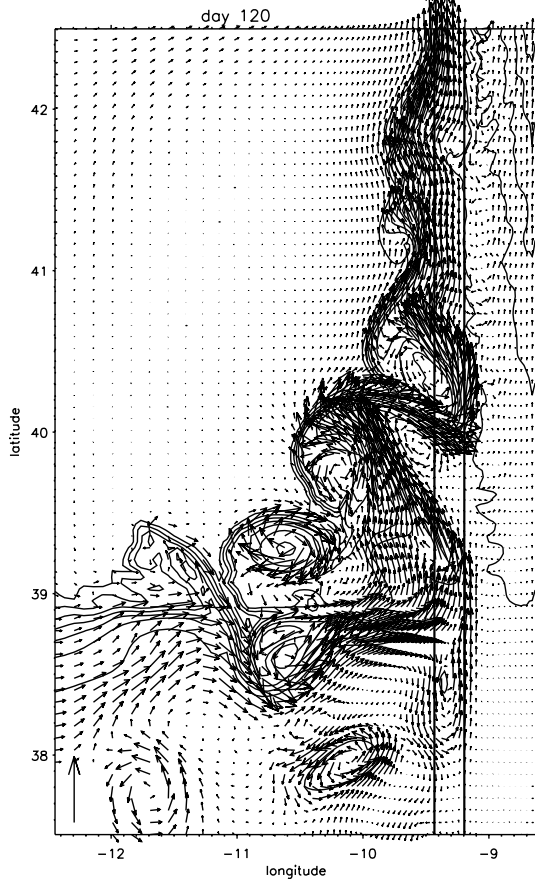
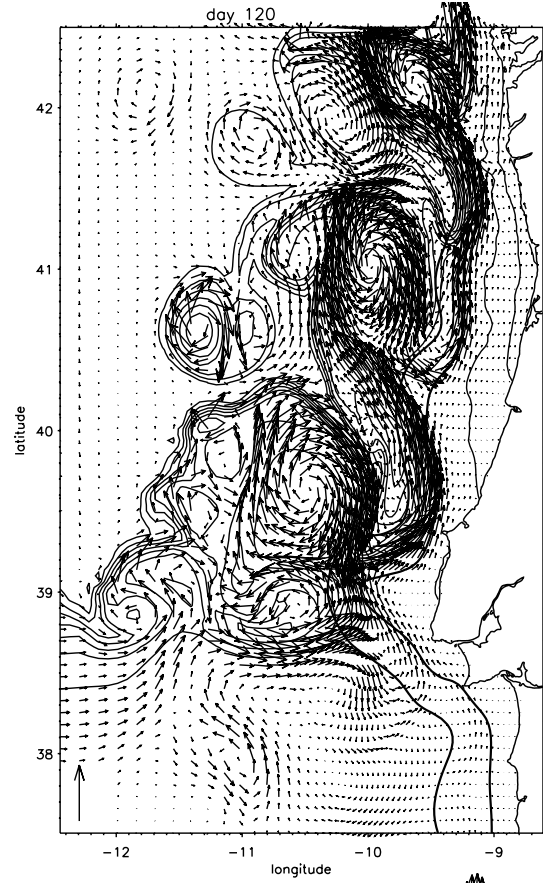
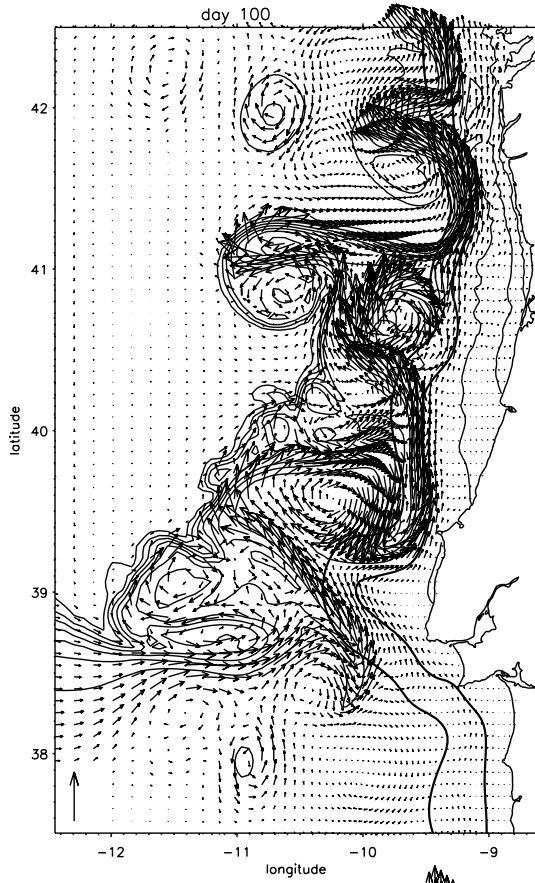


Figure 11. Depth of isopycnal surfaces (26.9 and 27.2) and isopycnal velocity (lighter shading corresponds to deeper pressure levels) in the zone of Aveiro Canyon showing the interaction, and separation of the dipoles. Velocity vectors are plotted with half of the resolution and are not in scale. Labels indicate the location of the eddies discussed in the text.



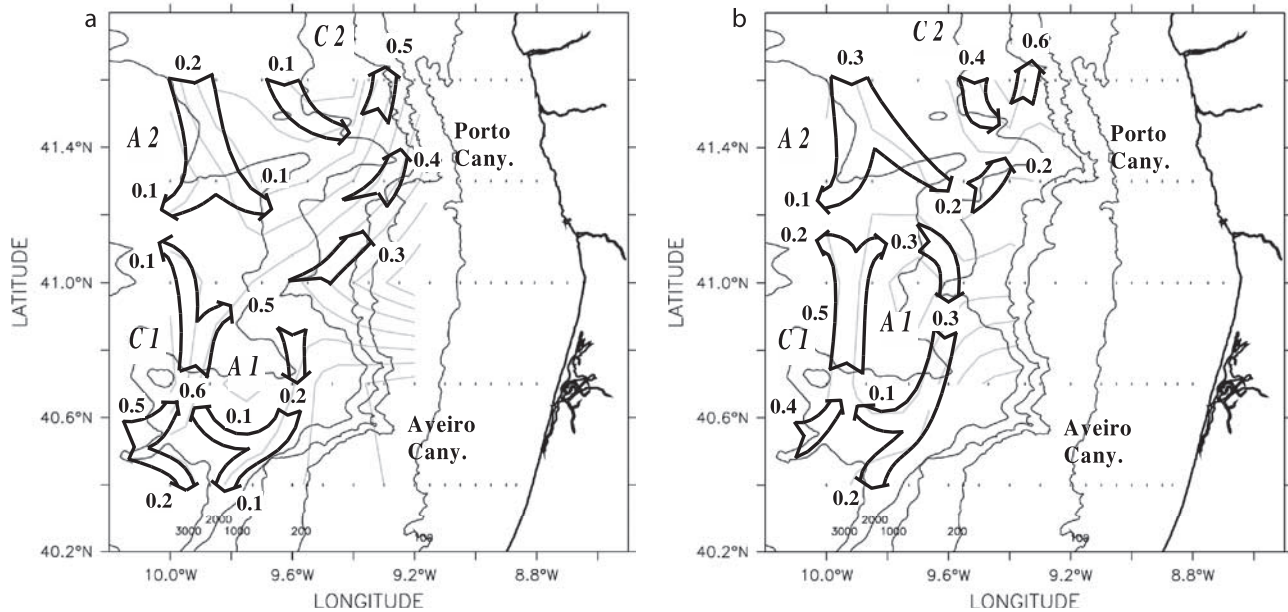


Figure 13. Scheme of the circulation features (cyclones C1/C2 and anticyclones A1/A2) estimated using the geostrophic calculations based on the high-resolution survey (dots indicate CTD stations) in the vicinity of Aveiro and Porto Canyons during February 2000. The plots correspond to transport estimates (bold numbers close to arrows in Sverdrups) obtained by integrating the geostrophic flow within two layers at Central Water levels and assuming a nondivergent condition. (a) The surface layer $\sigma_0 < 27.0$, (b) an intermediate layer $27.0 < \sigma_0 < 27.3$. Scheme adapted from *Oliveira et al.* [2003] study.

layer ($27.0\text{--}27.3 \sigma_\theta$). This fact is also noticeable in the structure of the modeled flow present in Figure 11.

[56] For a better evaluation of the flow structure obtained with the model, we make use of satellite SST data. Owing to the strong cloudiness in imagery off western Iberia during winter (peak of IPC activity), only a limited number of images are available for a systematic validation of the simulations. In addition, good sequences of images that could allow the assessment of some dynamical processes (like eddy shedding) are nonexistent. Consequently, the comparison of these simulations with real features is necessarily more qualitative, with a focus on the spatial structure and scales of the features.

[57] The most noticeable patterns in the winter imagery off Iberia (see Figure 1) are the thermal gradient, the deflection of the thermal front north-eastward in the CTZ, the isolation of the shelf waters (which are colder in this case), and the presence of trains of unstable structures in the CTZ. In Figure 14, two schematic representations provide an interpretation of some of the flow structures present in the images of Figure 1. It is possible to see that the zone of interaction of the meridional gradient with the slope is dominated by several turbulent structures, most of them dipolar. It is likely that these patterns are related to the adjustment of the meridional gradient to the slope. Keeping these in mind, there are some points of comparison with the

unstable structures obtained in the simulations that are discussed here, namely, (1) both are constituted by cyclone/anticyclone pairs (which is confirmed for most eddies in Figure 14); (2) the dominant anticyclones are of 60 to 70 km in diameter; (3) the offshore extension of the structures (the boundary of the CTZ in the images is located at about 11°W , approximately the same limit for the modeled CTZ); (4) the alignment of the axis of the dipolar vorticity structures (generally oriented north-westward) is comparable in both; and (5) the lengths between structures and some secondary features of the circulation in between, particularly some smaller eddies and cold intrusions, are alike in both the satellite and modeled surface temperature fields.

[58] Besides this qualitative comparison, the sea surface temperature fields of the advanced stages of the simulations (e.g., Figures 4 and 12, days 100–120) show several structures that can be compared with the images on an individual basis, e.g., the dipole stretched off-slope in the center of Figure 1a and in Figure 14 and the one in Figure 12, day 100 (described in section 4.3). There are also very similar aspects in the train of turbulent structures of Figure 1b which is comparable to those of Figure 12.

[59] Figures 15 and 16 show the evolution of two dipoles in the vicinity of Aveiro Canyon. The images are separated by 1 week. In the first image (Figure 15), corresponding to day 9 of January, it is possible to observe a meander to the

Figure 12. (opposite) (top) Surface temperature field (lines) and surface velocity vectors for the experiment with real topography (days 100 and 120). (bottom) Same fields for the experiment with meridionally invariant slope (for days 120 and 160). Minimum, maximum, and interval values are, respectively, 15.0, 16.2, and 0.2°C . A vector scale corresponding to 0.3 m s^{-1} is given in the lower left corner. The topography is represented by the 200- and 1000-m lines (thick lines).

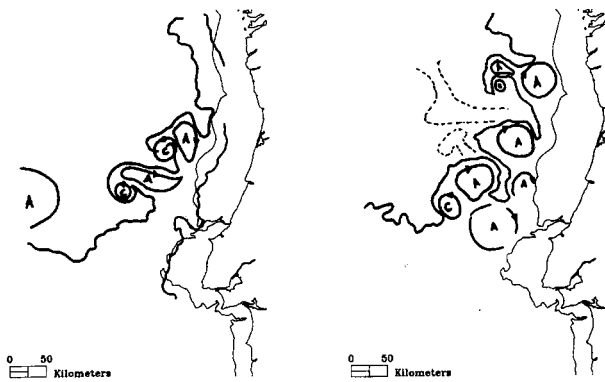


Figure 14. Schematic representation of some of the circulation features apparently conditioning the sea surface temperature distribution of the images presented in Figure 1. Thin lines represent the coastline and 200 m bathymetry. Thick lines represent the main fronts and eddies.

south of the canyon with an anticyclonic part to the north (A1) and cyclonic to the south (C1). Located inside the canyon, a smaller anticyclone with ~ 30 km diameter is observed (A2). After 1 week (Figure 16), both structures have evolved significantly. Apparently, they evolved into dipolar structures with a warmer core (anticyclonic part) and a colder sector likely associated with a cyclonic vorticity feature. The first structure, south of the canyon, may have evolved as a free unstable structure like those described in section 5. This is related to the fact that it has developed south of the canyon in a zone with straight slope. On the other hand, the structure inside the canyon may have been

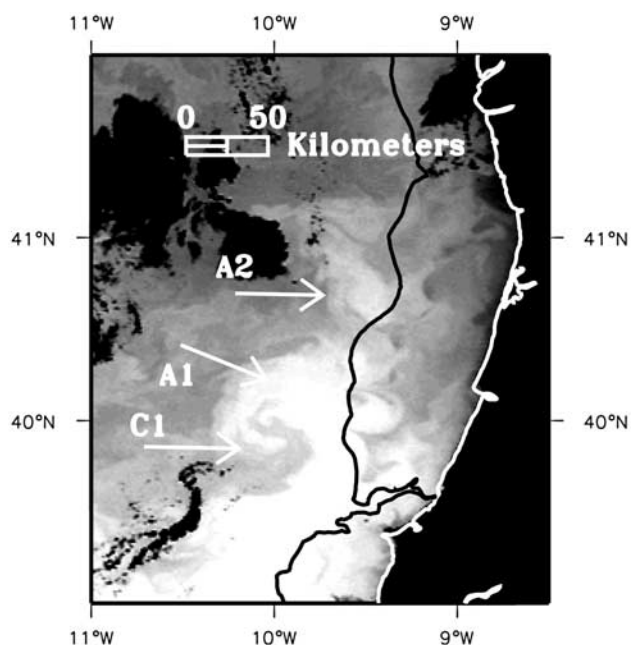


Figure 15. AVHRR brightness temperature image (09/01/2002, 0308 UTM) of the Western Iberia offshore. Shading corresponds to warm (lighter) and cold (darker) waters. Labels indicate eddies discussed in the text.

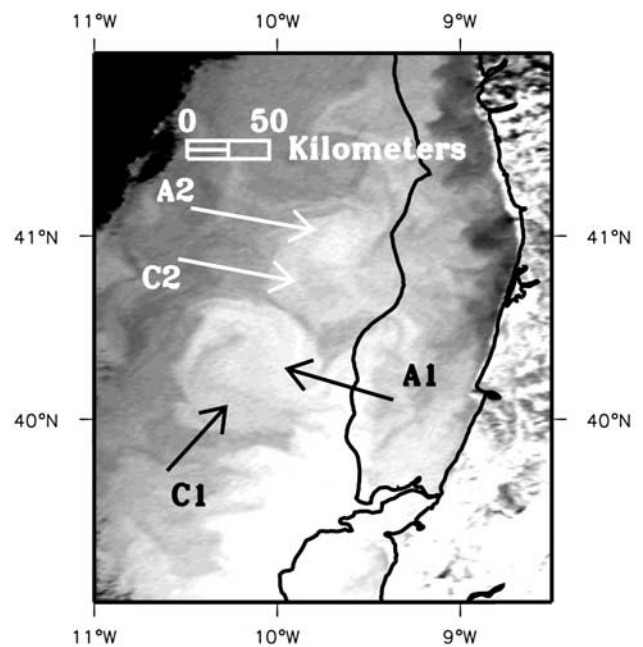


Figure 16. AVHRR brightness temperature image (16/01/2002, 1328 UTM) of the Western Iberia offshore. Shading corresponds to warm (lighter) and cold (darker) waters. Labels indicate eddies discussed in the text.

influenced by the topography, and the cyclone C2 (missing in the first image) may have generated in consequence to the deep cyclogenesis described in section 4.1.

7. Summary and Conclusions

[60] We have analyzed the adjustment of a meridional density gradient to a meridionally oriented slope, confirming that it is likely to be the central mechanism in the generation of the Iberian Poleward Current. The results show that this simple forcing in conjunction with a topography approximating the true bathymetry simulates many observed surface features in the zone. Among these are the generation of a Coastal Transition Zone, the change in orientation of the meridional gradient delimiting the CTZ, the trains of turbulent structures, and some detached eddies along the slope.

[61] It has been shown that a similar meridional gradient interacting with a meridionally invariant slope (with no canyons or promontories) also generates several vorticity structures with an accompanying degree of realism. However, it is noticed that the development of the structures is somewhat slower and less interaction between them occurs with no generation of detached structures.

[62] The role of the topographic features is to accelerate the development of eddy structures and instabilities and to introduce a diversity in scales. The second factor is probably decisive in increasing the tendency for different flow interactions creating the conditions for separation of eddies.

[63] Particular candidates for these interactions are the deep cyclones generated in the lee of the topography. It has been shown that the anticyclones generated in the process of separation most likely remain trapped to the slope.

However, in some cases, intensified cyclones shed as a result of the separation of the deep equatorward flow past topography or interaction with other vorticity structures may promote the separation of the anticyclones. Preferential locations for these interactions are the large canyons (like Aveiro Canyon) where the poleward slope flow (at the surface) may separate, generating negative vorticity structures (anticyclones) whereas the equatorward slope flow (in deeper layers) in the process of separation generates positive vorticity (cyclones).

[64] The described cyclogenesis occurs within the framework of sheared flow (poleward at the surface and equatorward at deeper levels). Unfortunately, in the case of Western Iberia, direct measurements of the slope currents are too rare and sparse to have conclusive information on the existence or nonexistence of such deeper equatorward currents. On the contrary, it is usually accepted that the surface poleward flow is vertically linked with the deep northward flowing Mediterranean Water which is not taken into account in the present experiments. In other systems like the Leeuwin Current, the undercurrent has been directly measured [Church *et al.*, 1989]. It should be noticed that the undercurrent is particularly discontinuous and that is probably why it has not been observed as a well-established pattern along the western Iberia slope. On the other hand, there is some evidence of southward flow in some across-slope density sections of Western Iberia margin [Oliveira *et al.*, 2003].

[65] In summary, it has been shown that many of the observed features of the Iberian Poleward Current may be explained by the interaction of a meridional density gradient with an approximated shelf/slope. The most relevant factors of this interaction are the generation of persistent anticyclones that remain trapped for long times and deep cyclogenesis in the lee of topography. These cyclones migrate poleward pushed by the stronger anticyclones promoting interaction among the different unstable structures, and in some cases contributing to eddy detachment. The study of these processes may contribute to the understanding of the generation of sweddies [Pingree and Le Cann, 1992; Dubert, 1998].

[66] **Acknowledgments.** This research was supported by the Portuguese Science Foundation (FCT) under contracts (FCT/PRAXIS/P/CTE/11282/98), project SURVIVAL and PELAGICOS. A large set of satellite imagery was browsed from the SeaMar project site of the PML satellite facility in UK. The authors appreciate the comments of the anonymous reviewers which were helpful to improve the manuscript.

References

- Arhan, M., A. C. de Verdière, and A. Mémerly, The eastern boundary of the subtropical North Atlantic, *J. Phys. Oceanogr.*, **24**, 1295–1316, 1994.
- Bormans, M., and C. Garrett, A simple criterion for gyre formation by the surface outflow from a strait, with application to the Alboran Sea, *J. Geophys. Res.*, **94**(C9), 12,637–12,644, 1989.
- Church, J. A., G. R. Cresswell, and J. S. Godfrey, The Leeuwin Current, in *Poleward Flows Along Eastern Ocean Boundaries, Coastal and Estuarine Stud.*, vol. 34, edited by S. J. Neshyba *et al.*, 374 pp., Springer-Verlag, New York, 1989.
- Dubert, J. P., Dynamique du Système de Courants vers le Pôle au Voisinage de la Pente Continentale à l'Ouest e au Nord de la Péninsule Ibérique, Ph.D. thesis, Univ. de Bretagne Occidentale, Brest, France, 1998.
- Durski, S., Physical-biological interactions in the Ocean: Modelling the effects of large and small-scale circulation simple planktonic systems, Ph.D. thesis, Rutgers Univ., New Brunswick, N. J., 2000.
- Frouin, R., A. F. G. Fiúza, I. Ambar, and T. J. Boyd, Observations of a poleward surface current off the coast of Portugal and Spain during winter, *J. Geophys. Res.*, **95**(C1), 679–691, 1990.
- Griffiths, R. W., and A. F. Pearce, Instability and eddy pairs in the Leeuwin Current south of Australia, *Deep Sea Res.*, **39**, 1511–1534, 1985.
- Haidvogel, D. B., and A. Beckman, *Numerical Ocean Circulation Modeling*, 318 pp., Imperial Coll. Press, River Edge, N. J., 1999.
- Haidvogel, D. B., H. G. Arango, K. Hedstrom, A. Beckmann, and A. F. Shchepetkin, Model evaluation experiments in the North Atlantic Basin: Simulations in nonlinear terrain-following coordinates, *Dyn. Atmos. Oceans*, **32**, 239–281, 2000.
- Haynes, R., and E. D. Barton, A Poleward flow along the Atlantic coast of the Iberian Peninsula, *J. Geophys. Res.*, **95**(C7), 11,425–11,441, 1990.
- Huthnance, J. M., Slope currents and “JEBAR,” *J. Phys. Oceanogr.*, **14**, 795–810, 1984.
- Huthnance, J. M., H. M. Van Aken, M. White, E. D. Barton, B. Le Cann, E. F. Coelho, E. A. Fanjul, P. Miller, and J. Vitorino, Ocean margin exchange-water flux estimates, *J. Mar. Syst.*, **32**, 107–137, 2002.
- Klinger, B. A., Baroclinic eddy generation at a sharp corner in a rotating system, *J. Geophys. Res.*, **99**(C6), 12,515–12,531, 1994a.
- Klinger, B. A., Inviscid current separation from rounded capes, *J. Phys. Oceanogr.*, **24**, 1805–1811, 1994b.
- Large, W. G., J. C. McWilliams, and S. C. Doney, Oceanic vertical mixing: A review and a model with nonlocal boundary layer parameterization, *Rev. Geophys.*, **32**, 363–403, 1994.
- Marchesiello, P., J. C. McWilliams, and A. Shchepetkin, Open boundary condition for long-term integration of regional oceanic models, *Ocean Modell.*, **3**, 1–20, 2000.
- Martins, C. S., M. Hamann, and A. F. G. Fiúza, Surface circulation in the eastern North Atlantic, from drifters and altimetry, *J. Geophys. Res.*, **107**(C12), 3217, doi:10.1029/2000JC000345, 2002.
- Mazé, J. P., M. Arhan, and H. Mercier, Volume budget of the eastern boundary layer off the Iberian Peninsula, *Deep Sea Res.*, **44**, 1543–1574, 1997.
- Nof, D., and T. Pichevin, The establishment of the Tsugaru and the Alboran Gyres, *J. Phys. Oceanogr.*, **29**, 39–54, 1999.
- Oliveira, P. B., A. Peliz, J. Dubert, T. Rosa, and A. M. Santos, Observations of mesoscale eddy field off Western Iberia in February 2000, *Deep Sea Res.*, in press, 2003.
- Pingree, R., and B. Le Cann, Three anticyclonic Slope Water Oceanic eDDIES (SWODDIEDS) in the southern Bay of Biscay in 1990, *Deep Sea Res.*, **39**, 1147–1175, 1992.
- Pingree, R., and B. Le Cann, A shallow Meddy (a Smeddy) from the secondary Mediterranean Salinity Maximum, *J. Geophys. Res.*, **98**(C11), 20,169–20,185, 1993.
- Pollard, R. T., and S. Pu, Structure and circulation of the upper Atlantic Ocean northeast of Azores, *Prog. Oceanogr.*, **14**, 443–462, 1985.
- Van Aken, H. M., The hydrography of the mid-latitude Northeast Atlantic Ocean: III., The subducted thermocline water mass, *Deep Sea Res., Part I*, **48**, 237–267, 2001.
- Weaver, A. J., and J. H. Middleton, On the dynamics of the Leeuwin Current, *J. Phys. Oceanogr.*, **19**, 625–648, 1989.
- Whitehead, J. A., and A. R. Miller, Laboratory simulation of the gyre in the Alboran Sea, *J. Geophys. Res.*, **84**(C7), 3733–3742, 1979.

J. Dubert, Departamento de Física, Universidade de Aveiro, 3810-194 Aveiro, Portugal. (jdubert@fis.ua.pt)

D. B. Haidvogel, Institute of Marine and Coastal Sciences, Rutgers University, 75 Dudley Road, New Brunswick, NJ 08901-8521, USA. (dale@imcs.rutgers.edu)

B. Le Cann, Laboratoire de Physique des Océans, CNRS/IFREMER/UBO, UFR Sciences 6, Avenue Le Gorgeu, BP 809 29285 Brest, France. (blcann@univ-brest.fr)

A. Peliz, IPIMAR-DAA, Avenida de Brasília, P-1449-006, Lisboa, Portugal. (apeliz@ipimar.pt)